Springer

Acta Mechanica Sinica

CrossMark click for updates

• RESEARCH PAPER •

Acta Mech. Sin., Vol. 41, 124096 (2025)
https://doi.org/10.1007/s10409-024-24096-x

Surface element design of nanomaterials considering surface curvature dependence

Yongchao Zhang[1], Lian Wang[1], Fangxin Wang[2], Bin Li[3], and Xiaofan Gou[1*]

[1] *College of Mechanics and Materials, Hohai University, Nanjing 211100, China;*
[2] *College of Architectural Science and Engineering, Yangzhou University, Yangzhou 225127, China;*
[3] *School of Mechanics and Photoelectric Physics, Anhui University of Science and Technology, Huainan 232001, China*

Received March 20, 2024; accepted April 15, 2024; published online September 12, 2024

Nanomaterials have garnered recognition for their notable surface effects and demonstration of superior mechanical properties. Previous studies on the surface effects of nanomaterials, employing the finite element method, often relied on simplified two-dimensional models due to theoretical complexities. Consequently, these simplified models inadequately represent the mechanical properties of nanomaterials and fail to capture the substantial impact of surface effects, particularly the curvature dependence of nanosurfaces. This study applies the principle of minimum energy and leverages the Steigmann-Ogden surface theory of nanomaterials to formulate a novel finite element surface element that comprehensively accounts for surface effects. We conducted an analysis of the stress distribution and deformation characteristics of four typical 2D and 3D nanomaterial models. The accuracy of the developed surface element and finite element calculation method was verified through comparison with established references. The resulting finite element model provides a robust and compelling scientific approach for accurately predicting the mechanical performance of nanomaterials.

Nanomaterials, Surface effect, Surface element, curvature dependence, Finite element method

Citation: Y. Zhang, L. Wang, F. Wang, B. Li, and X. Gou, Surface element design of nanomaterials considering surface curvature dependence, Acta Mech. Sin. 41, 124096 (2025), https://doi.org/10.1007/s10409-024-24096-x

1. Introduction

Classical elasticity theory is conventionally regarded as independent of both size and time. In macroscopic materials, where the surface area is significantly smaller in relation to their volume, the surface contribution is typically negligible, and only the mechanical properties of the bulk materials are taken into account [1,2]. However, as the size of a structure diminishes, the proportion of atoms located on the outermost layer gradually increases. The influence of the material's surfaces can no longer be dismissed at the nanoscale, unlike in macroscopic materials [3-6]. It is the strain energy contained within the surface and interface layers that gives rise to the notably distinct material properties exhibited by nanomaterials and nanostructures [7,8]. This phenomenon, attributed to the elevated specific surface area of nanomaterials, is denoted as the surface effects [9].

To incorporate surface effects into a mechanical framework, Gurtin and Murdoch developed a surface elasticity model that encompasses both surface tensile and shear stresses [10,11]. Their model conceptualizes the nanosurfaces as a two-dimensional film adhering to the three-dimensional substrate materials [12,13]. Subsequently, Steigmann and Ogden [14,15] supplemented the Gurtin-Murdoch model and introduced a new surface model capable of accommodating out-of-plane bending deformation of nanosurfaces.

Following the pioneering research outlined above, the theoretical examination of surface effects on nanomaterials transitioned toward application in various mechanical scenarios. Initially, mechanical properties including deflection, deformation, and Young's modulus of nanomaterials with straightforward physical structures like nanowires [16-19], nanobeams [20,21], nanoplates [22], and nanofilms [23,24]

*Corresponding author. E-mail address: xfgou@hhu.edu.cn (Xiaofan Gou)
Executive Editor: Xiaoyan Li

were extensively investigated. Scholars also delved into the analysis of stress perturbations [25,26], stress concentrations [27-29], stress distributions [30-33], displacement distributions [34,35], and the mechanical behaviors of indenters in both idealized infinite elastic space and elastic half-space problems. Moreover, the alignment and combination of one-dimensional nanobeams in space enabled the creation of mechanical metamaterials with markedly enhanced mechanical properties. The reinforcing influences of surface effects on the equivalent Young's modulus and bending behavior were demonstrated in classical open- and closed-hole Gibson-Ashby models [36], the Kelvin model [37], and their hierarchical structures [38,39]. Utilizing interface phase models or cohesion models to predict equivalent elastic properties offers valuable insights into characterizing nanomaterial interfaces [40,41].

In addition to theoretical approaches, molecular dynamics methods have demonstrated effectiveness in capturing microstructural surface effects by tracking atomic interactions [42-45]. However, for nanomaterials with feature sizes in the range of several hundred nanometers or larger, traditional molecular dynamics methods become computationally expensive, leading to reduced efficiency [46]. On the other hand, the finite element method, rooted in continuous medium mechanics principles, provides higher computational efficiency and greater flexibility in mesh density. Nevertheless, conventional finite element methods face challenges in accurately simulating nanoscale mechanical behavior due to a lack of formulations capable of accounting for microstructural surface effects [47-50]. A few researchers are working towards modeling the mechanical response of nanosurfaces by adapting surface finite elements. For instance, Wei et al. [51] investigated the mechanical properties of two-dimensional nanomaterials by integrating one-dimensional surface elements into a standard finite element program. Similarly, Wang et al. [52] and Tian and Rajapakse [53] employed a comparable approach to study stress concentration near two-dimensional circular nanovoids.

The preceding studies employing the finite element method to assess the mechanical properties of nanomaterials have predominantly relied on relatively straightforward two-dimensional computational models. Consequently, these models fall short in capturing the mechanical response of nanostructures in the z-direction and fail to account for the significant influence of surface effects. Despite the proposal of the Steigmann-Ogden model over two decades ago, the impact of surface bending stiffness on nanosurfaces has seldom been addressed in the existing literature, both in theoretical analyses and numerical simulations. Consequently, the investigations aimed at capturing surface effects in three-dimensional nanostructures while considering the dependence on nanosurface curvature remain notably scarce. This study aims to develop a novel surface element and formulate a robust multi-scale computational method that integrates surface curvature stiffness, enabling a comprehensive understanding of the surface behavior exhibited by two- and three-dimensional nanomaterials with diverse structural geometries. The present paper is structured as follows: Sect. 2 details the construction of the novel nanosurface element. In Sect. 3, we scrutinize the stress distribution and displacement characteristics of several typical nanomaterials to validate the accuracy of the surface element and finite element calculation method established in Sect. 4. Lastly, Sect. 4 encapsulates the primary conclusions drawn from this research endeavor.

2. Model and method

2.1 System energy equations

Consider a deformable region V encompassing a nano interface or surface Γ (if no differentiation is stipulated, interface and surface in the latter case are uniformly denominated as surface). We assume that V is subjected to a prescribed body force $\mathbf{b}$ and a surface traction $\mathbf{t}$ along the outer boundary (S_t), as illustrated in Fig. 1. The total potential energy of this system, denoted as Π, is a combination of three constituent components: the strain energy of the matrix material, denoted as U^M, the strain energy of the surface, denoted as U^F, and the mechanical work performed by external forces, represented as W. This relationship can be mathematically represented as follows:

$$\Pi = U^M + U^F + W. \tag{1}$$

The principle of minimum energy ensures that the variation in the total energy of the system is zero. This leads to the reformulation of Eq. (1) as follows:

$$\delta\Pi = 0. \tag{2}$$

Within the framework of linear elastic materials, each component in Eq. (1) is expressed as follows:

$$\begin{cases} U^M = \int_V \gamma^M \mathrm{d}V, \\ U^F = \int_\Gamma \gamma^F \mathrm{d}S, \\ W = -\int_V \mathbf{u}\cdot\mathbf{b}\mathrm{d}V - \int_{S_t} \mathbf{u}\cdot\mathbf{t}\mathrm{d}S, \end{cases} \tag{3}$$

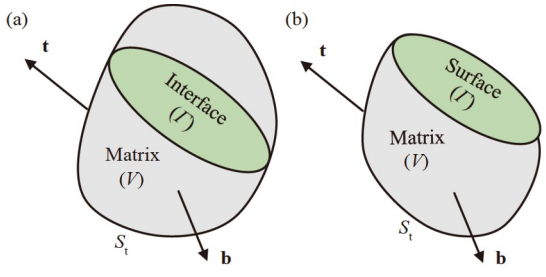

Figure 1 Schematic of nano systems: (a) interface and (b) surface.

where $\mathbf{u}$ represents the displacement vector. γ^{M} and γ^{F} represent the elastic energy density of the matrix and surface. Building upon the Steigmann-Ogden surface model [14,15]. we can further specify these quantities as follows:

$$\gamma^{\mathrm{M}} = \frac{1}{2}\boldsymbol{\varepsilon}^{\mathrm{M}} : \mathbf{D}^{\mathrm{M}} : \boldsymbol{\varepsilon}^{\mathrm{M}}, \tag{4}$$

$$\gamma^{\mathrm{F}} = \gamma_0 + \boldsymbol{\tau}^{\mathrm{F}} : \boldsymbol{\varepsilon}^{\mathrm{F}} + \frac{1}{2}\boldsymbol{\varepsilon}^{\mathrm{F}} : \mathbf{D}^{\mathrm{F}} : \boldsymbol{\varepsilon}^{\mathrm{F}} + \frac{1}{2}c_{\mathrm{F}}\boldsymbol{\kappa}^{\mathrm{F}} : \mathbf{C}^{\mathrm{F}} : \boldsymbol{\kappa}^{\mathrm{F}}, \tag{5}$$

where γ_0 and $\boldsymbol{\tau}^{\mathrm{F}}$ represent the free energy density and residual stress tensor of the surface, respectively. $\boldsymbol{\varepsilon}^{\mathrm{M}}$, $\boldsymbol{\varepsilon}^{\mathrm{F}}$ and $\boldsymbol{\kappa}^{\mathrm{F}}$ represent matrix strain tensor, surface strain tensor, and change of surface curvature tensor, respectively. $\mathbf{D}^{\mathrm{M}}$, $\mathbf{D}^{\mathrm{F}}$ and $\mathbf{C}^{\mathrm{F}}$ denote matrix elastic stiffness tensor, surface tensile stiffness tensor, and surface bending stiffness tensor, respectively. The Gurtin-Murdoch model can be regarded as the Steigmann-Ogden model, under the assumption of neglecting the contribution of surface bending stiffness. Thus, we utilize the coefficient, c_{F}, to differentiate between the two surface models. When c_{F} is equal to 0, it pertains to the Gurtin-Murdoch model [10,11], whereas when c_{F} is equal to 1, it pertains to the Steigmann-Ogden surface model [14,15].

By incorporating Eqs. (4) and (5) into Eq. (3), we can derive the variational equations corresponding to each distinct type of energy:

$$\begin{cases} \delta U^{\mathrm{M}} = \int_V \boldsymbol{\varepsilon}^{\mathrm{M}} : \mathbf{D}^{\mathrm{M}} : \delta\boldsymbol{\varepsilon}^{\mathrm{M}} \mathrm{d}V, \\ \delta U^{\mathrm{F}} = \int_\Gamma \left(\boldsymbol{\tau}^{\mathrm{F}} : \delta\boldsymbol{\varepsilon}^{\mathrm{F}} + \boldsymbol{\varepsilon}^{\mathrm{F}} : \mathbf{D}^{\mathrm{F}} : \delta\boldsymbol{\varepsilon}^{\mathrm{F}} + c_{\mathrm{F}}\boldsymbol{\kappa}^{\mathrm{F}} : \mathbf{C}^{\mathrm{F}} : \delta\boldsymbol{\kappa}^{\mathrm{F}}\right)\mathrm{d}S, \\ \delta W = -\int_V \mathbf{b}\cdot\delta\mathbf{u}\mathrm{d}V - \int_{S_{\mathrm{t}}} \mathbf{t}\cdot\delta\mathbf{u}\mathrm{d}S. \end{cases} \tag{6}$$

The equations, as delineated in Eq. (6), serve as the foundational basis for the subsequent derivation.

2.2 Element equilibrium equations

This section is dedicated to formulating a systematic approach to derive the equilibrium equations that govern the system's components based on the foundational principles elucidated in Sect. 2.1. The methodology we adopt involves applying the classical technique of piecewise interpolation. This is used to describe displacement and strain across the diverse elements of the system, encompassing both the matrix and surface domains. This is encapsulated in the equation below:

$$\begin{cases} \mathbf{u}_{\mathrm{M}} = \mathbf{N}_{\mathrm{M}}\boldsymbol{\delta}^{\mathrm{e}}_{\mathrm{M}}, \\ \mathbf{u}_{\mathrm{F}} = \mathbf{N}_{\mathrm{F}}\boldsymbol{\delta}^{\mathrm{e}}_{\mathrm{F}}, \end{cases} \tag{7}$$

$$\begin{cases} \boldsymbol{\varepsilon}_{\mathrm{M}} = \mathbf{B}_{\mathrm{M}}\boldsymbol{\delta}^{\mathrm{e}}_{\mathrm{M}}, \\ \boldsymbol{\varepsilon}_{\mathrm{F}} = \mathbf{B}_{\mathrm{F}}\boldsymbol{\delta}^{\mathrm{e}}_{\mathrm{F}}, \end{cases} \tag{8}$$

where $\mathbf{N}_{\mathrm{M}}$ and $\mathbf{N}_{\mathrm{F}}$ denote the shape function of the matrix and surface elements, respectively. Likewise, $\mathbf{B}_{\mathrm{M}}$ and $\mathbf{B}_{\mathrm{F}}$ denote the strain matrix of the matrix and surface elements, respectively. $\boldsymbol{\delta}^{\mathrm{e}}_{\mathrm{M}}$ and $\boldsymbol{\delta}^{\mathrm{e}}_{\mathrm{F}}$ denote nodal displacement of the matrix and surface elements. Especially, the nodal displacements of the matrix elements and surface elements satisfy the following equation:

$$\boldsymbol{\delta}^{\mathrm{e}}_{\mathrm{M}} = \mathbf{T}^{-1}\boldsymbol{\delta}^{\mathrm{e}}_{\mathrm{F}}. \tag{9}$$

The transformation matrix $\mathbf{T}$ in Eq. (9) represents the projection from the comprehensive global frame to the localized frame. It succinctly denotes the complex transformation that occurs within the elemental nodal displacement components.

By substituting Eqs. (7)-(9) into Eqs. (2) and (6), the finite element format for the system energy equation can be obtained

$$\begin{aligned} &\int_V \mathbf{B}_{\mathrm{M}} : \mathbf{D}^{\mathrm{M}} : \mathbf{B}_{\mathrm{M}}\boldsymbol{\delta}^{\mathrm{e}}_{\mathrm{M}}\mathrm{d}V \\ &+\int_\Gamma \Big(\mathbf{B}_{\mathrm{FT}}\mathbf{T} : \boldsymbol{\tau}^{\mathrm{F}} + \mathbf{B}_{\mathrm{FT}}\mathbf{T} : \mathbf{D}^{\mathrm{F}} : \mathbf{B}_{\mathrm{FT}}\mathbf{T}\boldsymbol{\delta}^{\mathrm{e}}_{\mathrm{M}} \\ &+c_{\mathrm{F}}\mathbf{B}_{\mathrm{FB}}\mathbf{T} : \mathbf{C}^{\mathrm{F}} : \mathbf{B}_{\mathrm{FB}}\mathbf{T}\boldsymbol{\delta}^{\mathrm{e}}_{\mathrm{M}}\Big)\mathrm{d}S \\ &-\int_V \mathbf{N}_{\mathrm{M}} : \mathbf{b}\mathrm{d}V - \int_{S_{\mathrm{t}}} \mathbf{N}_{\mathrm{M}} : \mathbf{t}\mathrm{d}S = 0, \end{aligned} \tag{10}$$

where $\mathbf{B}_{\mathrm{FT}}$ and $\mathbf{B}_{\mathrm{FB}}$ denote tensile and bending components in the strain matrix of the surface elements. Then, the element equilibrium equations in discrete systems can be derived as follows:

$$\left(c_1\mathbf{K}^{\mathrm{e}}_{\mathrm{M}} + c_2\mathbf{K}^{\mathrm{e}}_{\mathrm{F}}\right)\boldsymbol{\delta}^{\mathrm{e}}_{\mathrm{M}} = \mathbf{f}, \tag{11}$$

$$\begin{cases} \mathbf{K}^{\mathrm{e}}_{\mathrm{M}} = \int_V \mathbf{B}_{\mathrm{M}} : \mathbf{D}^{\mathrm{M}} : \mathbf{B}_{\mathrm{M}}\mathrm{d}V, \\ \mathbf{K}^{\mathrm{e}}_{\mathrm{F}} = \int_\Gamma \left(\mathbf{B}_{\mathrm{FT}}\mathbf{T} : \mathbf{D}^{\mathrm{F}} : \mathbf{B}_{\mathrm{FT}}\mathbf{T} + c_{\mathrm{F}}\mathbf{B}_{\mathrm{FB}}\mathbf{T} : \mathbf{C}^{\mathrm{F}} : \mathbf{B}_{\mathrm{FB}}\mathbf{T}\right)\mathrm{d}S, \\ \mathbf{f} = \int_V \mathbf{N}_{\mathrm{M}} : \mathbf{b}\mathrm{d}V + \int_{S_{\mathrm{t}}} \mathbf{N}_{\mathrm{M}} : \mathbf{t}\mathrm{d}S - c_2\int_\Gamma \mathbf{B}_{\mathrm{F}}\mathbf{T} : \boldsymbol{\tau}^{\mathrm{F}}\mathrm{d}S, \end{cases} \tag{12}$$

where $\mathbf{f}$ represents the element nodal force. $\mathbf{K}^{\mathrm{e}}_{\mathrm{M}}$ and $\mathbf{K}^{\mathrm{e}}_{\mathrm{F}}$ denote the stiffness matrix for both the matrix and surface elements. The constants c_1 and c_2 are defined as follows: for matrix elements, c_1 equals 1 and c_2 equals 0; conversely, for surface elements, c_1 equals 0 and c_2 equals 1. It is worth noting that we adopt the conventional approach towards surface residual stresses, regarding them as one part of the element nodal forces in conjunction with the external loads. In fact, Eqs. (11) and (12) are important theoretical supports of the approach of constructing surface elements to emulate surface effects.

2.3 Finite element equations of two-dimensional model

The surface within a two-dimensional nanostructure can be discretized as one-dimensional elements, as can be seen in

Fig. 2(a). The Gurtin-Murdoch model posits that the nanosurface is a zero-thickness film capable only of withstanding tensile deformations, while the Steigmann-Ogden model considers the bending characteristics of the nanosurface. Thus, based on their deformation characteristics, we innovatively categorize one-dimensional surface according to the Gurtin-Murdoch model and Steigmann-Ogden model as truss and beam elements, as can be seen in Fig. 2(b) and (c).

The nodal displacement of the truss element can be expressed in the local and global coordinate systems as $\boldsymbol{\delta}_{\mathrm{F}}^{\mathrm{e}}$ and $\overline{\boldsymbol{\delta}}_{\mathrm{F}}^{\mathrm{e}}$. The relationship between the two nodal displacements is satisfied by

$$\boldsymbol{\delta}_{\mathrm{S}}^{\mathrm{e}} = \mathbf{T}\overline{\boldsymbol{\delta}}_{\mathrm{S}}^{\mathrm{e}}, \tag{13}$$

where the coordinate transformation matrix satisfies the following equation:

$$\mathbf{T} = \begin{bmatrix} \cos\varphi & \sin\varphi & 0 & 0 \\ -\sin\varphi & \cos\varphi & 0 & 0 \\ 0 & 0 & \cos\varphi & \sin\varphi \\ 0 & 0 & -\sin\varphi & \cos\varphi \end{bmatrix}. \tag{14}$$

It is imperative to acknowledge that the nodal displacements of the surface element must align with the corresponding matrix element in the global coordinate system to ensure deformation compatibility. Hence, the element strain matrix $\overline{\mathbf{B}}_{\mathrm{F}}$ and element stiffness matrix $\overline{\mathbf{K}}_{\mathrm{F}}^{\mathrm{e}}$ can be derived in the global coordinate system through the application of coordinate transformation, as illustrated in the subsequent expression:

$$\overline{\mathbf{B}}_{\mathrm{F}} = \begin{bmatrix} -\dfrac{\cos\varphi}{l_{\mathrm{truss}}} & -\dfrac{\sin\varphi}{l_{\mathrm{truss}}} & \dfrac{\cos\varphi}{l_{\mathrm{truss}}} & \dfrac{\sin\varphi}{l_{\mathrm{truss}}} \end{bmatrix}, \tag{15}$$

$$\overline{\mathbf{K}}_{\mathrm{F}}^{\mathrm{e}} = \frac{E_{\mathrm{truss}}A_{\mathrm{truss}}}{l_{\mathrm{truss}}} \begin{bmatrix} \cos\varphi\cos\varphi & \sin\varphi\cos\varphi & -\cos\varphi\cos\varphi & -\sin\varphi\cos\varphi \\ \sin\varphi\cos\varphi & \sin\varphi\sin\varphi & -\sin\varphi\cos\varphi & -\sin\varphi\sin\varphi \\ -\cos\varphi\cos\varphi & -\sin\varphi\cos\varphi & \cos\varphi\cos\varphi & \sin\varphi\cos\varphi \\ -\sin\varphi\cos\varphi & -\sin\varphi\sin\varphi & \sin\varphi\cos\varphi & \sin\varphi\sin\varphi \end{bmatrix}, \tag{16}$$

where E_{truss}, A_{truss}, and l_{truss} represent the elastic modulus, cross sectional area, and length of the truss element, respectively.

The axial force of the truss element and the 2D constitutive relation of the nano surface based on the Gurtin-Murdoch model can be expressed as

$$N_{\mathrm{truss}} = E_{\mathrm{truss}}A_{\mathrm{truss}}\varepsilon_{\mathrm{truss}}, \tag{17}$$

$$\sigma^{\mathrm{F}} = (\lambda_0 + 2\mu_0 - \tau_0)\varepsilon^{\mathrm{F}} + \tau_0, \tag{18}$$

where $\varepsilon_{\mathrm{truss}}$ represents the axial strain of the truss element. σ^{F} and ε^{F} represent surface stress and strain. τ_0 represents surface residual stress. λ_0 and μ_0 represent the surface Lamé constants. Comparing Eq. (17) with Eq. (18), it is not difficult to derive the following relationship:

$$E_{\mathrm{truss}}A_{\mathrm{truss}} = (\lambda_0 + 2\mu_0 - \tau_0)l_{\mathrm{truss}}. \tag{19}$$

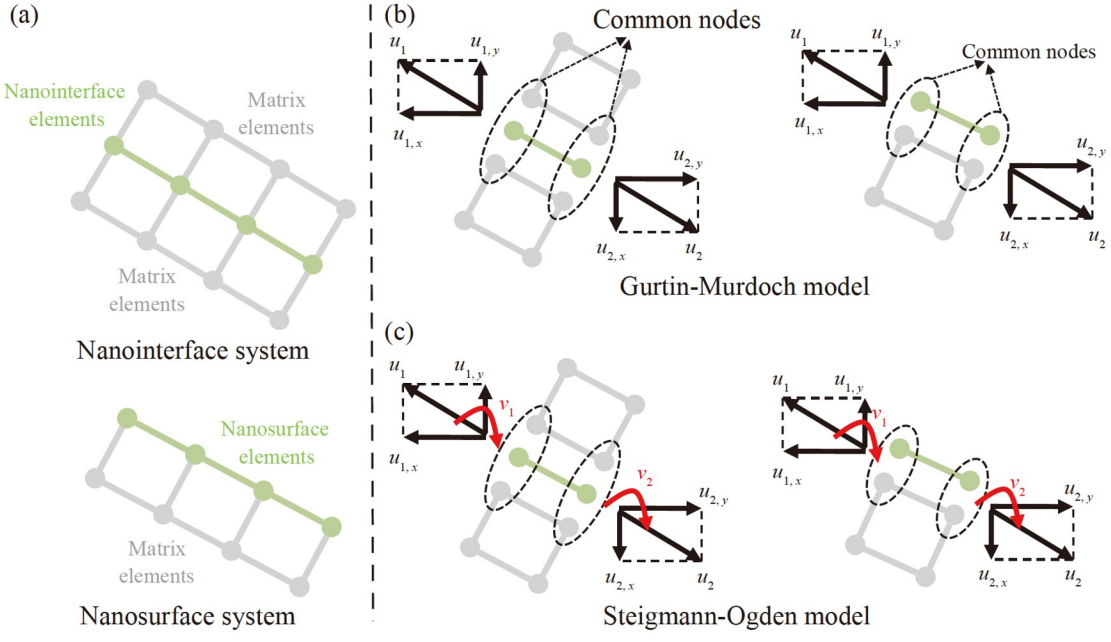

Figure 2 Diagram of 2D (a) nanosurface systems considering, (b) Gurtin-Murdoch model, and (c) Steigmann-Ogden model.

Using a similar approach, we can obtain the coordinate transformation matrix of the beam element. The strain matrix and stiffness matrix of the beam element in the global coordinate system can be expressed as

$$\mathbf{T}=\begin{bmatrix} \cos\varphi & \sin\varphi & 0 & 0 & 0 & 0 \\ -\sin\varphi & \cos\varphi & 0 & 0 & 0 & 0 \\ 0 & 0 & 1 & 0 & 0 & 0 \\ 0 & 0 & 0 & \cos\varphi & \sin\varphi & 0 \\ 0 & 0 & 0 & -\sin\varphi & \cos\varphi & 0 \\ 0 & 0 & 0 & 0 & 0 & 1 \end{bmatrix}, \tag{20}$$

$$\overline{\mathbf{B}}_{\mathrm{F}}=\begin{bmatrix} B_{11} & B_{12} & B_{13} & B_{14} & B_{15} & B_{16} \\ B_{21} & B_{22} & B_{23} & B_{24} & B_{25} & B_{26} \end{bmatrix}, \tag{21}$$

$$\overline{\mathbf{K}}_{\mathrm{F}}^{\mathrm{e}}=\begin{bmatrix} K_{11} & K_{12} & K_{13} & K_{14} & K_{15} & K_{16} \\ K_{21} & K_{22} & K_{23} & K_{24} & K_{25} & K_{26} \\ K_{31} & K_{32} & K_{33} & K_{34} & K_{35} & K_{36} \\ K_{41} & K_{42} & K_{43} & K_{44} & K_{45} & K_{45} \\ K_{51} & K_{52} & K_{53} & K_{54} & K_{55} & K_{56} \\ K_{61} & K_{62} & K_{63} & K_{64} & K_{65} & K_{66} \end{bmatrix}. \tag{22}$$

The submatrices in Eqs. (21) and (22) can be expressed as

$$\begin{aligned} &B_{11}=-\frac{\cos\varphi}{l_{\mathrm{beam}}},\ B_{12}=-\frac{\sin\varphi}{l_{\mathrm{beam}}},\ B_{13}=0,\ B_{14}=\frac{\cos\varphi}{l_{\mathrm{beam}}},\\ &B_{15}=\frac{\sin\varphi}{l_{\mathrm{beam}}},\ B_{16}=0,\ B_{21}=-\left(-\frac{6}{l_{\mathrm{beam}}^2}+\frac{12}{l_{\mathrm{beam}}^3}x\right)\sin\varphi,\\ &B_{22}=\left(-\frac{6}{l_{\mathrm{beam}}^2}+\frac{12}{l_{\mathrm{beam}}^3}x\right)\cos\varphi,\ B_{23}=\frac{4}{l_{\mathrm{beam}}}-\frac{6}{l_{\mathrm{beam}}^2}x,\\ &B_{24}=-\left(\frac{6}{l_{\mathrm{beam}}^2}-\frac{12}{l_{\mathrm{beam}}^3}x\right)\sin\varphi,\ B_{25}=\left(\frac{6}{l_{\mathrm{beam}}^2}-\frac{12}{l_{\mathrm{beam}}^3}x\right)\cos\varphi,\\ &B_{26}=\frac{2}{l_{\mathrm{beam}}}-\frac{6}{l_{\mathrm{beam}}^2}x, \end{aligned} \tag{23}$$

$$\begin{aligned} K_{11}&=-K_{41}=-K_{14}=K_{44}\\ &=\frac{E_{\mathrm{beam}}A_{\mathrm{beam}}}{l_{\mathrm{beam}}}\cos\varphi\cos\varphi+\frac{12E_{\mathrm{beam}}I_{\mathrm{beam}}}{l_{\mathrm{beam}}^3}\sin\varphi\sin\varphi,\\ K_{22}&=-K_{52}=-K_{25}=K_{55}\\ &=\frac{E_{\mathrm{beam}}A_{\mathrm{beam}}}{l_{\mathrm{beam}}}\sin\varphi\sin\varphi+\frac{12E_{\mathrm{beam}}I_{\mathrm{beam}}}{l_{\mathrm{beam}}^3}\cos\varphi\cos\varphi,\\ K_{13}&=K_{16}=-K_{43}=-K_{46}=K_{31}=K_{61}=-K_{34}=-K_{64}\\ &=\frac{6E_{\mathrm{beam}}I_{\mathrm{beam}}}{l_{\mathrm{beam}}^2}\sin\varphi,\\ K_{23}&=K_{26}=-K_{53}=-K_{56}=K_{32}=K_{62}=-K_{35}=-K_{65}\\ &=-\frac{6E_{\mathrm{beam}}I_{\mathrm{beam}}}{l_{\mathrm{beam}}^2}\cos\varphi,\\ K_{12}&=-K_{42}=-K_{15}=K_{45}=K_{21}=-K_{51}=-K_{24}=K_{54}\\ &=\frac{E_{\mathrm{beam}}A_{\mathrm{beam}}}{l_{\mathrm{beam}}}\cos\varphi\sin\varphi-\frac{12E_{\mathrm{beam}}I_{\mathrm{beam}}}{l_{\mathrm{beam}}^3}\sin\varphi\cos\varphi,\\ K_{33}&=K_{66}=2K_{36}=2K_{63}=\frac{4E_{\mathrm{beam}}I_{\mathrm{beam}}}{l_{\mathrm{beam}}}. \end{aligned} \tag{24}$$

The bending moment of the beam element and the 2D constitutive relation of the nano surface based on the Steigmann-Ogden model can be expressed as

$$M_{\mathrm{beam}}=E_{\mathrm{beam}}I_{\mathrm{beam}}\kappa_{\mathrm{beam}}, \tag{25}$$

$$M^{\mathrm{F}}=(\xi_0+2\eta_0)\kappa^{\mathrm{F}}, \tag{26}$$

where κ_{truss} represents the curvature of the beam element. M^{F} and κ^{F} represent surface bending moment and curvature. ξ_0 and η_0 denote a set of constants that measure the bending stiffness of the surface. Comparing Eq. (25) with Eq. (26), it is not difficult to derive the following relationship:

$$E_{\mathrm{beam}}I_{\mathrm{beam}}=(\xi_0+2\eta_0)l_{\mathrm{beam}}. \tag{27}$$

Eqs. (19) and (27) delineate the conversion relationship between the material parameters of the truss/beam elements and the surface of 2D nano structures, respectively. Incorporating this conversion relation into the derived strain and stiffness matrices of the surface elements facilitates the construction of these elements.

2.4 Finite element equations of three-dimensional model

In contrast to the 2D scenario, the surface of 3D nano structures can be discretized into 2D elements. Considering the deformation characteristics of the nano surface, we advocate employing a three-node triangular planar element to simulate surface elasticity in accordance with the Gurtin-Murdoch model, as shown in Fig. 3(a). Furthermore, the surface elasticity considering the Steigmann-Ogden model is replicated by overlaying a layer of four-node rectangular thin plate elements onto three-node triangular face elements, as shown in Fig. 3(b).

The coordinate transformation matrix of a three-node triangular planar element satisfies the following equation:

$$\begin{cases} \mathbf{T}=\begin{bmatrix} \mathbf{T}_1 & 0 & 0 \\ 0 & \mathbf{T}_1 & 0 \\ 0 & 0 & \mathbf{T}_1 \end{bmatrix}, \\ \mathbf{T}_1=\begin{bmatrix} a_{11} & a_{21} & a_{31} \\ a_{12} & a_{22} & a_{32} \\ a_{13} & a_{23} & a_{33} \end{bmatrix}, \end{cases} \tag{28}$$

where a_{rs} denotes the projection of the basis vectors of the local coordinate system along the basis vectors of the global coordinate system. Thus, the element strain matrix $\overline{\mathbf{B}}_{\mathrm{F}}$ and element stiffness matrix $\overline{\mathbf{K}}_{\mathrm{F}}^{\mathrm{e}}$ can be derived in the global coordinate system through the application of coordinate transformation, as illustrated in the following expression:

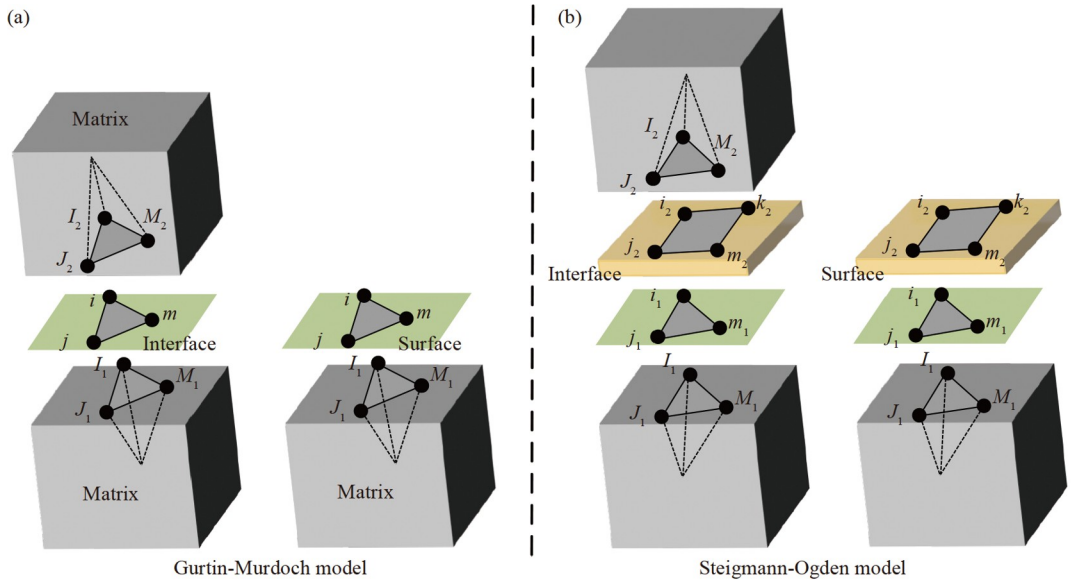

Figure 3 Diagram of 3D nanosurface systems considering (a) Gurtin-Murdoch model and (b) Steigmann-Ogden model.

$$\overline{\mathbf{B}}_{\mathrm{F}}=\frac{1}{2A_{\mathrm{tri}}}\begin{bmatrix} b_i a_{11} & b_i a_{21} & b_i a_{31} & b_j a_{11} \\ c_i a_{12} & c_i a_{22} & c_i a_{32} & c_j a_{12} \\ c_i a_{11}+b_i a_{12} & c_i a_{21}+b_i a_{22} & c_i a_{31}+b_i a_{32} & c_j a_{11}+b_j a_{12} \end{bmatrix}$$
$$\begin{bmatrix} b_j a_{21} & b_j a_{31} & b_m a_{11} & b_m a_{21} & b_m a_{31} \\ c_j a_{22} & c_j a_{32} & c_m a_{12} & c_m a_{22} & c_m a_{32} \\ c_j a_{21}+b_j a_{22} & c_j a_{31}+b_j a_{32} & c_m a_{11}+b_m a_{12} & c_m a_{21}+b_m a_{22} & c_m a_{31}+b_m a_{32} \end{bmatrix}, \tag{29}$$

$$\overline{\mathbf{K}}_{\mathrm{F}}^{\mathrm{e}}=\overline{\mathbf{B}}_{\mathrm{F}}^{\mathrm{T}}\mathbf{D}_{\mathrm{tri}}\overline{\mathbf{B}}_{\mathrm{F}}t_{\mathrm{tri}}A_{\mathrm{tri}}, \tag{30}$$

where t_{tri}, $\mathbf{D}_{\mathrm{tri}}$ and A_{tri} denote the thickness, elastic stiffness matrix, and the area of the three-node triangular planar element. b_i and c_i represent a set of constants. These values can be expressed as follows:

$$\mathbf{D}_{\mathrm{tri}}=\frac{E_{\mathrm{tri}}}{1-\nu_{\mathrm{tri}}^2}\begin{bmatrix} 1 & \nu_{\mathrm{tri}} & 0 \\ \nu_{\mathrm{tri}} & 1 & 0 \\ 0 & 0 & (1-\nu_{\mathrm{tri}})/2 \end{bmatrix}, \tag{31}$$

$$A_{\mathrm{tri}}=\frac{1}{2}\begin{vmatrix} 1 & x'_i & y'_i \\ 1 & x'_j & y'_j \\ 1 & x'_m & y'_m \end{vmatrix}, \tag{32}$$

$$\begin{cases} b_i=y'_j-y'_m, \\ c_i=-x'_j+x'_m, \end{cases} \quad i,j,m, \tag{33}$$

where E_{tri} and ν_{tri} are the elastic modulus and Poisson's ratio of the three-node triangular planar elements. The symbols "i, j, m" in Eq. (33) represent the subscript rotation operation.

The constitutive relation of the three-node triangular planar element and 3D nanosurface based on the Gurtin-Murdoch model can be expressed as

$$\boldsymbol{\sigma}_{\mathrm{tri}}=\mathbf{D}_{\mathrm{tri}}\boldsymbol{\varepsilon}_{\mathrm{tri}}, \tag{34}$$

$$\boldsymbol{\sigma}^{\mathrm{F}}=\tau_0\mathbf{I}_{\mathrm{F}}+2(\mu_0-\tau_0)\mathbf{I}_{\mathrm{F}}\boldsymbol{\varepsilon}^{\mathrm{F}}+(\lambda_0+\tau_0)(\mathrm{tr}\boldsymbol{\varepsilon}^{\mathrm{F}})\mathbf{I}_{\mathrm{F}}, \tag{35}$$

where $\mathbf{I}_{\mathrm{F}}$ denotes the surface unit tensor. Comparing Eq. (34) with Eq. (35), it is not difficult to derive the following relationship:

$$\begin{cases} E_{\mathrm{tri}}=\dfrac{4(\mu_0+\lambda_0)(\mu_0-\tau_0)}{(2\mu_0+\lambda_0-\tau_0)t_{\mathrm{tri}}}, \\ \nu_{\mathrm{tri}}=\dfrac{\lambda_0+\tau_0}{2\mu_0+\lambda_0-\tau_0}. \end{cases} \tag{36}$$

Using a similar approach, we can obtain the coordinate transformation matrix of the four-node rectangular thin plate element, the strain matrix and the stiffness matrix in the global coordinate system:

$$\begin{cases} \mathbf{T}=\begin{bmatrix} \mathbf{T}_2 & 0 & 0 & 0 \\ 0 & \mathbf{T}_2 & 0 & 0 \\ 0 & 0 & \mathbf{T}_2 & 0 \\ 0 & 0 & 0 & \mathbf{T}_2 \end{bmatrix}, \\ \mathbf{T}_2=\begin{bmatrix} \mathbf{T}_1 & 0 \\ 0 & \mathbf{T}_1 \end{bmatrix}, \end{cases} \tag{37}$$

$$
\begin{cases}
\overline{\mathbf{B}}_{\mathrm{F}}=\left[\overline{\mathbf{B}}_i \quad \overline{\mathbf{B}}_j \quad \overline{\mathbf{B}}_m \quad \overline{\mathbf{B}}_k\right], \\
\overline{\mathbf{B}}_r=\dfrac{1}{4ab}\left[\overline{\mathbf{B}}_{r1} \quad \overline{\mathbf{B}}_{r2} \quad \overline{\mathbf{B}}_{r3} \quad \overline{\mathbf{B}}_{r4} \quad \overline{\mathbf{B}}_{r5} \quad \overline{\mathbf{B}}_{r6}\right], \quad r=i,j,m,k, \\
\overline{\mathbf{B}}_{r1}=\begin{bmatrix} 3\dfrac{b}{a}\xi_r\xi(1+\eta_r\eta)a_{13} \\ 3\dfrac{a}{b}\eta_r\eta(1+\xi_r\xi)a_{13} \\ \xi_r\eta_r(3\xi^2+3\eta^2-4)a_{13}\end{bmatrix}, \overline{\mathbf{B}}_{r2}=\begin{bmatrix} 3\dfrac{b}{a}\xi_r\xi(1+\eta_r\eta)a_{23} \\ 3\dfrac{a}{b}\eta_r\eta(1+\xi_r\xi)a_{23} \\ \xi_r\eta_r(3\xi^2+3\eta^2-4)a_{23}\end{bmatrix}, \\
\overline{\mathbf{B}}_{r3}=\begin{bmatrix} 3\dfrac{b}{a}\xi_r\xi(1+\eta_r\eta)a_{33} \\ 3\dfrac{a}{b}\eta_r\eta(1+\xi_r\xi)a_{33} \\ \xi_r\eta_r(3\xi^2+3\eta^2-4)a_{33}\end{bmatrix}, \overline{\mathbf{B}}_{r4}=\begin{bmatrix} b\xi_r(1+3\xi_r\xi)(1+\eta_r\eta)a_{12} \\ -a\eta_r(1+\xi_r\xi)(1+3\eta_r\eta)a_{11} \\ -b\xi_r\left(3\eta^2+2\eta_r\eta-1\right)a_{11}+a\eta_r\left(3\xi^2+2\xi_r\xi-1\right)a_{12}\end{bmatrix}, \\
\overline{\mathbf{B}}_{r5}=\begin{bmatrix} b\xi_r(1+3\xi_r\xi)(1+\eta_r\eta)a_{22} \\ -a\eta_r(1+\xi_r\xi)(1+3\eta_r\eta)a_{21} \\ -b\xi_r\left(3\eta^2+2\eta_r\eta-1\right)a_{21}+a\eta_r\left(3\xi^2+2\xi_r\xi-1\right)a_{22}\end{bmatrix}, \\
\overline{\mathbf{B}}_{r6}=\begin{bmatrix} b\xi_r(1+3\xi_r\xi)(1+\eta_r\eta)a_{32} \\ -a\eta_r(1+\xi_r\xi)(1+3\eta_r\eta)a_{31} \\ -b\xi_r\left(3\eta^2+2\eta_r\eta-1\right)a_{31}+a\eta_r\left(3\xi^2+2\xi_r\xi-1\right)a_{32}\end{bmatrix}, \quad r=i,j,m,k,
\end{cases} \tag{38}
$$

$$
\overline{\mathbf{K}}_{\mathrm{F}}^{\mathrm{e}}=ab\int_{-1}^{1}\int_{-1}^{1}\overline{\mathbf{B}}_{\mathrm{F}}^{\mathrm{T}}\mathbf{D}_{\mathrm{rec}}\overline{\mathbf{B}}_{\mathrm{F}}^{\mathrm{T}}\mathrm{d}\xi\mathrm{d}\eta, \tag{39}
$$

where $\mathbf{T}_1$ denotes the submatrix of the coordinate transformation matrix in Eq. (28). The coefficients a and b are half of the length and width of the four-node rectangular thin plate element. For ease of Gaussian integration, we establish a local coordinate system denoted as C, where the origin is set at the center of the rectangular thin plate element. ξ and η are employed as the horizontal and vertical coordinates, respectively. The coordinates of the four nodes of the element under local coordinate system C are denoted as ξ_r and η_r, and they satisfy the following relation:

$$
\begin{cases}
\xi_i=-1,\ \eta_i=-1, \\
\xi_j=1,\ \eta_j=-1, \\
\xi_m=1,\ \eta_m=1, \\
\xi_k=-1,\ \eta_k=1.
\end{cases} \tag{40}
$$

The constitutive relation of the four-node rectangular thin plate element and the 3D constitutive relation of the nanosurface based on the Steigmann-Ogden model can be expressed as

$$
\mathbf{M}_{\mathrm{rec}}=\mathbf{D}_{\mathrm{rec}}\boldsymbol{\kappa}_{\mathrm{rec}}, \tag{41}
$$

$$
\mathbf{D}_{\mathrm{rec}}=\frac{E_{\mathrm{rec}}t_{\mathrm{rec}}^3}{12(1-v_{\mathrm{rec}}^2)}\begin{bmatrix} 1 & v_{\mathrm{rec}} & 0 \\ v_{\mathrm{rec}} & 1 & 0 \\ 0 & 0 & (1-v_{\mathrm{rec}})/2\end{bmatrix}, \tag{42}
$$

$$
\mathbf{M}^{\mathrm{F}}=\xi_0\mathrm{tr}(\boldsymbol{\kappa}^{\mathrm{F}})\mathbf{I}_{\mathrm{F}}+2\eta_0\boldsymbol{\kappa}^{\mathrm{F}}, \tag{43}
$$

where E_{rec}, v_{rec} and t_{rec} are elastic modulus, Poisson's ratio and thickness of the four-node rectangular thin plate element, respectively. Comparing Eq. (41) with Eq. (43), it is not difficult to derive the following relationship:

$$
\begin{cases}
E_{\mathrm{rec}}t_{\mathrm{rec}}^3=\dfrac{48\eta_0(\xi_0+\eta_0)}{\xi_0+2\eta_0}, \\
v_{\mathrm{rec}}=\dfrac{\xi_0}{\xi_0+2\eta_0}.
\end{cases} \tag{44}
$$

Equations (36) and (44) delineate the conversion relationship between the material parameters of the three-node triangular planar elements (or the four-node rectangular thin plate elements) and the surface of the 3D nanostructures, respectively. The construction of the surface elements can be further accomplished by taking the above parameter relationships into the strain and stiffness matrices of the surface elements.

2.5 Secondary development of programs

The FORTRAN programming language is employed to construct a surface element to facilitate data exchange between the main solver and the user element. The specific steps are outlined below: (1) build the matrix elements; (2) get the global coordinates of the surface nodes; (3) construct the coordinate transformation matrix; (4) initialize the stiffness matrix of the surface elements; (5) construct the

strain matrix, the elasticity matrix and the stiffness matrix of the surface elements; (6) calculate stress and strain of the surface elements; (7) construct element balance equations; (8) calculate, iterate and update data.

3. Results and discussions

To validate the accuracy of the developed surface elements and finite element calculation method, we analyze the stress distributions and deformation characteristics of various 2D and 3D models. Subsequently, we compare these calculations with the corresponding references. The specific models under discussion comprise: a 2D simply supported plate, a 2D infinite plane with a circular void, a 3D soft solid containing liquid inclusion, and a 3D half space subjected to normal traction.

3.1 2D simply supported plate

As can be seen in Fig. 4(a), we focus on the transverse displacement v of a simply supported plate under plane strain subjected to a distributed pressure $p(x) = p_0 \sin(\pi x / w)$, where p_0 is the peak pressure magnitude of 5 MPa. The plate's width w and thickness t_0 are 0.2 μm and 10 nm, respectively. The Young's modulus E_b and Poisson's ratio ν_b of the matrix are 78 GPa and 0.42. The surface residual stress τ_0, surface Lamé constants λ_0 and μ_0 are 1 N/m, 5 N/m and 10 N/m, respectively [22]. The selected material parameters align with the theoretical solutions employed for comparison. The mesh of the matrix is accomplished using three-node linear plane-strain triangular elements (CPE3) in ABAQUS, while upper and lower nanosurfaces are discretized by truss elements. The number of elements in the model is 16000 and the calculation time is around 5 min.

The cases 0, 1, 2, and 3 correspond, respectively, to scenarios without surface effects ($\tau_0 = \lambda_0 = \mu_0 = 0$), with only surface tension ($\tau_0 \neq 0$ and $\lambda_0 = \mu_0 = 0$), with only surface elasticity ($\tau_0 = 0$, $\lambda_0 \neq 0$ and $\mu_0 \neq 0$), and with both effects ($\tau_0 \neq 0$, $\lambda_0 \neq 0$ and $\mu_0 \neq 0$). In Fig. 4(b), the finite element calculations closely align with the theoretical values [54]. The accuracy of the developed finite element calculation method is very high, which is attributed to the model is not complex. The transverse displacements in Fig. 4(b) reveal that the surface effects tend to increase the stiffness of the simply supported plate under the selected nanosurface parameter conditions. In particular, the surface residual stress exerts a greater influence on model hardening compared to the surface Lamé constant. This phenomenon aligns with our earlier observations regarding Young's modulus in nanoporous metals [55].

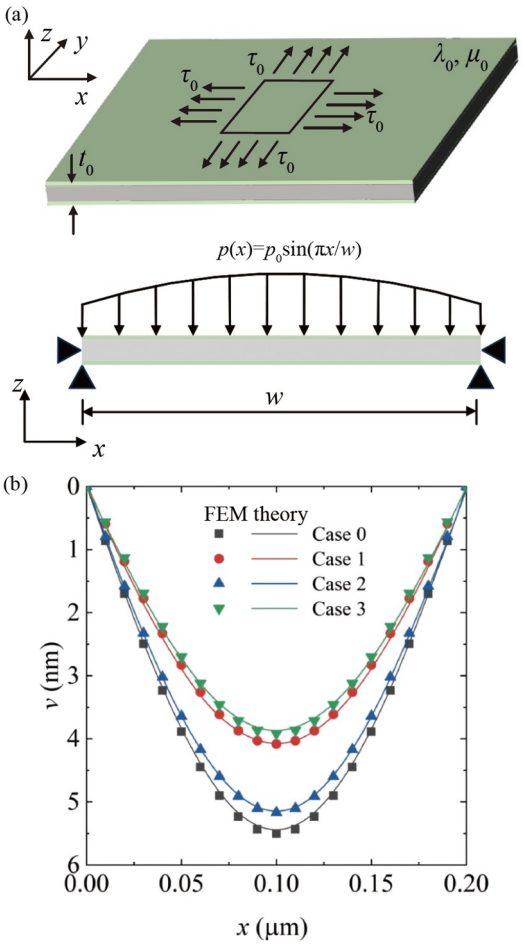

Figure 4 Simply supported plate under plane strain. (a) Diagram of the model; (b) transverse displacements.

3.2 2D plane with circular void

To address the influence of surface curvature, in this section, we examine the stress distribution around a nanoscale circular void with a radius of R_0 = 10 nm subjected to uniaxial tension of p_y = 100 MPa along the y-direction, as shown in Fig. 5(a). In the convenience of finite element analysis, we adopt a quarter model which constraints the x-direction displacement of the nodes at the negative x-direction boundary, and the y-direction displacement of the nodes at the negative y-direction boundary, depicted in Fig. 5(b). To eliminate boundary effects, the square side length is set to 20 times the diameter of the void.

Analytical solutions for comparisons were provided by Sharma et al. [13] for the Gurtin-Murdoch model and by Zemlyanova and Mogilevskaya [56] for the Steigmann-Ogden model. The matrix material chosen was freshly cut aluminum, characterized by a Young's modulus E_b = 70 GPa and a Poisson's ratio ν_b = 0.35. Additionally, the surface parameters are as follows: surface residual stress τ_0 is 0.911 N/m, surface Lamé constant λ_0 is 6.851 N/m, and μ_0 is −0.376 N/m [53]. However, as of now, widely accepted

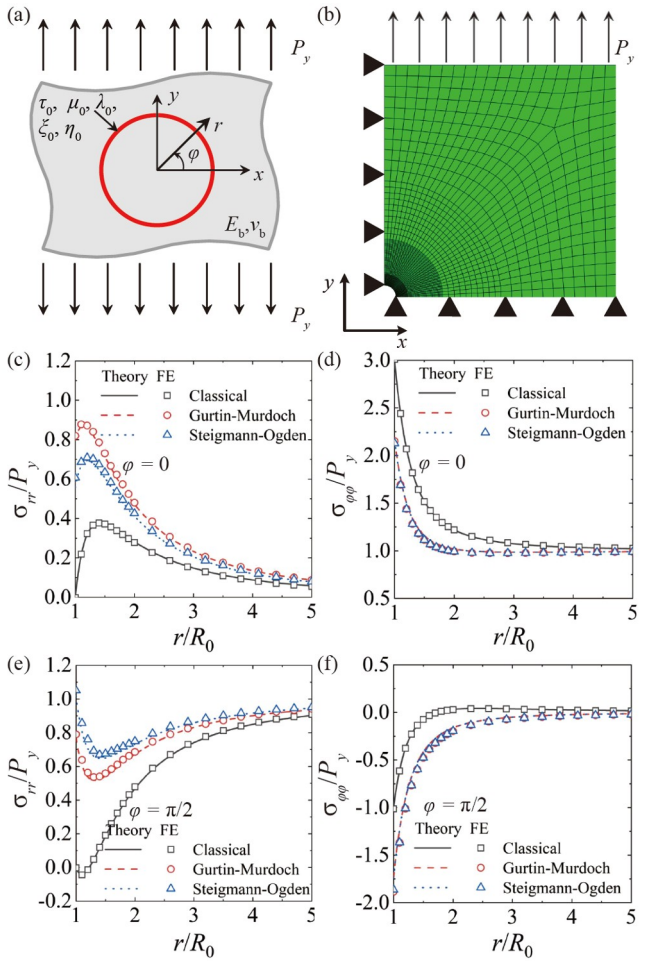

Figure 5 2D infinite plane with circular void: (a) configuration of the model; (b) diagram of finite element mesh. Distribution of (c) radial stress at $\varphi = 0$, (d) hoop stress at $\varphi = 0$, (e) radial stress at $\varphi = \pi/2$, and (f) hoop stress at $\varphi = \pi/2$.

surface bending constants in Eq. (27) have yet to be established for nanomaterials. Consequently, to merely delineate the influence trend of the surface bending constants on the stress field surrounding nano voids, we assume a surface bending constant of $\eta_0 = \xi_0 = 500$ nN nm [52,57]. The mesh of the matrix is accomplished using eight-node quadratic plane strain elements (CPE8R) in ABAQUS, while nanosurfaces are discretized using beam elements. The number of elements in the model is 10000 and the calculation time is around 4 min.

The hollow scattering points in Fig. 5(c)-(f) accurately align with the curves depicting the analytical solutions, affirming the precision of the finite element program in capturing the mechanical behavior of nanosurfaces. Notably, the surface effects augment the radial stress in proximity to the circular nanovoid. Nevertheless, the surface curvature still has a tendency to flatten the radial stress curve. On the other hand, the hoop stress is contingent upon location. Specifically, at $\varphi = 0$, the surface effect diminishes hoop tensile stress, while at $\varphi = \pi/2$, it amplifies hoop compressive stress. It is evident that considering the surface curvature has minimal impact on the hoop stress. Moreover, as the observation position moves farther from the void, the impact of the surface effects diminishes gradually, becoming nearly negligible when the observation position exceeds five times the void diameter.

3.3 3D soft solids with liquid inclusion

A recent discovery in elastocapillary reveals that a soft solid containing liquid inclusions can exhibit greater stiffness compared to its counterpart lacking such inclusions, owing to the influence of surface tension on the solid [58,59]. Figure 6(a) depicts a 3D model of a droplet within an extensive solid domain subjected to far-field strains, with 1/8 of the total domain analyzed due to symmetry considerations. l and w represent the major and minor diameters of the deformed droplet, respectively, while the liquid is assumed to be incompressible. The incompressible soft solid possesses a Young's modulus of 1.7 kPa, and the surface tension is denoted as $\tau_0 = 3.6$ mN/m [58]. To eliminate the effects of the border, the ratio between the edge size of the cube and the radius of the sphere is set at 20. The matrix elements comprise the quadratic tetrahedral elements, whereas the surface elements consist of the three-node triangular planar elements, resulting in a total of approximately 500000 elements. The calculation time of every model is around 30 min. We utilize the numerical predictions by He and Park [60] as well as the theoretical and experimental findings by Style et al. [58] for comparison with our computations.

Figure 6(b) and (c) depict the aspect ratio l/w of liquid inclusion under two displacement loading conditions. Specifically, Conditions 1 is $\varepsilon_{xx} = 5.6\%$ and $\varepsilon_{yy} = -1.5\%$, and Conditions 2 is $\varepsilon_{xx} = 17.5\%$ and $\varepsilon_{yy} = -2.6\%$. Our predictions align more closely with the theoretical solution curves compared to those of He and Park [60]. This discrepancy arises from our comprehensive consideration of surface residual stress in the Young's modulus and Poisson's ratio of our element, which is in contrast to He et al.'s [60] approach. Given the discrete nature of the experiments, our numerical predictions exhibit some deviation from the experimental results, but the overall trend remains remarkably consistent. Moreover, as the size of the liquid inclusions increases, the aspect ratio l/w stabilizes, signifying a reduction in the influence of the surface effects.

3.4 3D half space with a normal traction

In this section, we analyze a simplified scenario involving a uniform normal traction (p_0) applied within a circular boundary of radius (R_0) on the elastic half space. To mitigate boundary effects, we construct a finite element model of a

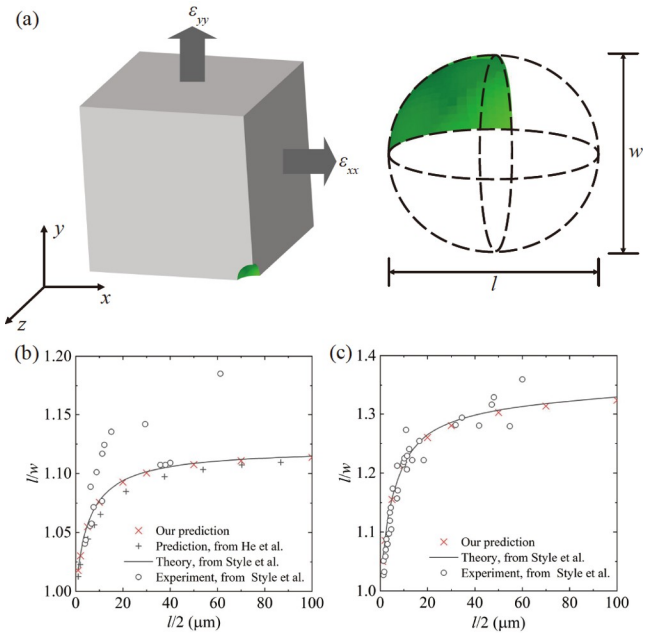

Figure 6 Soft solid stiffened by a liquid inclusion: (a) 1/8 of the 3D model. Aspect ratio l/w of liquid inclusion under far-field strains (b) ε_{xx} = 5.6 % and ε_{yy} = −1.5 %, and (c) ε_{xx} = 17.5 % and ε_{yy} = −2.6 %.

cubic elastomer with side lengths 20 times the radius, depicted in Fig. 7(a). Surface effects are specifically analyzed on the top surface of the cube, while the remaining surfaces are left untreated. The half space solid is modeled as an isotropic aluminum material. Consequently, the matrix materials and the Lamé constants of the surface match those outlined in Sect. 3.2. The constant G_b in Fig. 7(b)-(d) indicates the shear modulus of the matrix. The comparative data is sourced from theoretical solutions advanced by Mi

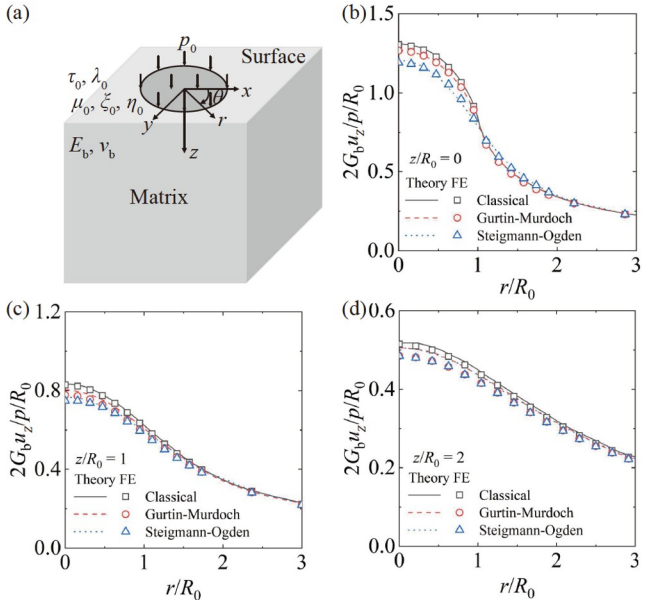

Figure 7 3D elastic half-space subjected to a normal traction over a nano sized circular area: (a) configuration of the model. Distribution of vertical displacement u_z at (b) z/R_0 = 0, (c) z/R_0 = 1, and (d) z/R_0 = 2.

[30], so the surface bending constants are also consistent with them ($\xi_0 = 2\eta_0$ = 1 nN nm). The number of elements in the model is 300000 and the calculation time is around 20 min.

Figure 7(b)-(d) shows the distribution of vertical displacement u_z at z/R_0 = 0, 1 and 2, respectively. The computational outcomes obtained through the finite element method closely align with the theoretical values at observation positions of z/R_0 = 0 and 1, with a slight increase in error observed at z/R_0 = 2. This is primarily attributed to the significant distance between the observation position and the loading surface, thereby amplifying the effect of the perturbation. Nonetheless, the computational errors remain minimal overall (below 3%), attesting to the continued high accuracy of the developed computational method. Observably, the curvatures of all nine displacement curves undergo a sign change along the circular loading boundary. Both surface models contribute to augmenting the absolute values of the radii of curvature at all three depths. Consequently, they collectively contribute to the smoothing of the displacement curves, particularly when accounting for surface curvature.

4. Concluding remarks

This study facilitates the creation of a finite element calculation model proficient in accounting for curvature-dependent surface effects in 2D and 3D nanostructures, achieved by innovating finite elements tailored for nano surfaces. We formulated the stiffness matrix for the novel surface element and established the correlation between the nanosurface parameters and the surface element parameters. The accuracy of the developed surface element and finite element calculation method is verified by calculating the stress distribution and deformation characteristics of typical 2D and 3D models and comparing them with the references. We found that the surface residual stress exerts a greater influence on model hardening compared to the surface Lamé constant. Besides, a soft solid containing liquid inclusions can exhibit greater stiffness compared to its counterpart lacking such inclusions, owing to the influence of surface tension on the solid. Moreover, the surface effects, particularly when accounting for surface curvature, contribute to augmenting the absolute values of the radii of displacement curvature on 3D elastic half space subjected to a normal traction.

It is important to acknowledge that the finite element computational model developed in this paper has certain limitations. For instance, it currently lacks the capability to simulate crack extension, rendering it applicable solely to perfect interfaces. Furthermore, the interface elements constructed in the model are designed with very small thick-

nesses, aiming to minimize the influence of element thickness on the mechanical properties of nanostructures to the greatest extent possible.

Data availability

Data will be made available on request.

Conflict of interest *On behalf of all authors, the corresponding author states that there is no conflict of interest.*

Author contributions ***Yongchao Zhang****: Conceptualization, Methodology, Model and Writing — original draft.* ***Lian Wang****: Model and Methodology.* ***Fangxin Wang****: Model and Review.* ***Bin Li****: Code and Example.* ***Xiaofan Gou****: Laboratory Management, Supervision and Edit.*

Acknowledgements *This work was supported by the Jiangsu Funding Program for Excellent Postdoctoral Talent (Grant No. 2023ZB397), and the Project funded by China Postdoctoral Science Foundation (Grant No. 2023M732986).*

1 M. R. Kired, B. E. Hachi, D. Hachi, and M. Haboussi, Effects of nano-voids and nano-cracks on the elastic properties of a host medium: XFEM modeling with the level-set function and free surface energy, Acta Mech. Sin. **35**, 799 (2019).
2 C. Fan, K. Liu, Y. Wang, L. Zhang, and L. Sun, Nano-indentation and nano-scratch of flexible intraocular lens material at the molecular scale, Acta Mech. Sin. **39**, 122331 (2023).
3 Y. Shi, W. Yang, Q. Bai, J. Qin, and Z. Zhang, Alloying/dealloying mechanisms, microstructural modulation and mechanical properties of nanoporous silver via a liquid metal-assisted alloying/dealloying strategy, J. Alloys Compd. **872**, 159675 (2021).
4 A. Yao, H. Yang, J. Q. Wang, W. Xu, J. Huo, R. W. Li, H. Qiu, and M. Chen, Flexible supercapacitor electrodes fabricated by dealloying nanocrystallized Al-Ni-Co-Y-Cu metallic glasses, J. Alloys Compd. **772**, 164 (2019).
5 M.A. Eltaher, and N. Mohamed, Nonlinear stability and vibration of imperfect CNTs by Doublet mechanics, Appl. Math. Comput. **382**, 125311 (2020).
6 A. Imani Aria, and H. Biglari, Computational vibration and buckling analysis of microtubule bundles based on nonlocal strain gradient theory, Appl. Math. Comput. **321**, 313 (2018).
7 E. S. Sergeeva, Dependence of the elastic properties of a single-walled carbon nanotube on its chirality, Solid State Phenom. **284**, 20 (2018).
8 B. Kocak, and Y. O. Ciftci, The effect of pressure on structural, electronic, elastic, vibration and optical properties of ScXSb (X=Ni, Pd, Pt) compounds, Comput. Condensed Matter **14**, 176 (2018).
9 L. Zhang, Z. Jing, Z. Li, and T. Fujita, Surface defects improved SERS activity of nanoporous gold prepared by electrochemical dealloying, Nanomaterials **13**, 187 (2023).
10 M. E. Gurtin, and A. Ian Murdoch, A continuum theory of elastic material surfaces, Arch. Rational Mech. Anal. **57**, 291 (1975).
11 M. E. Gurtin, J. Weissmuller, and F. Larche, A general theory of curved deformable interface in solids at equilibrium, Philos. Mag. A-Phys. Condens. Matter Struct. Defect Mech. Prop. **78**, 1093 (1998).
12 P. Sharma, and S. Ganti, Size-dependent eshelby's tensor for embedded nano-inclusions incorporating surface/interface energies, J. Appl. Mech. **71**, 663 (2005).
13 P. Sharma, S. Ganti, and N. Bhate, Effect of surfaces on the size-dependent elastic state of nano-inhomogeneities, Appl. Phys. Lett. **82**, 535 (2003).
14 D. J. Steigmann, and R. W. Ogden, Plane deformations of elastic solids with intrinsic boundary elasticity, Proc. R. Soc. Lond. A **453**, 853 (1997).
15 D. J. Steigmann, and R. W. Ogden, Elastic surface-substrate interactions, Proc. R. Soc. Lond. A **455**, 437 (1999).
16 G. F. Wang, and X. Q. Feng, Effects of surface elasticity and residual surface tension on the natural frequency of microbeams, Appl. Phys. Lett. **90**, 231904 (2007).
17 J. He, and C. M. Lilley, Surface effect on the elastic behavior of static bending nanowires, Nano Lett. **8**, 1798 (2008).
18 G. F. Wang, and X. Q. Feng, Surface effects on buckling of nanowires under uniaxial compression, Appl. Phys. Lett. **94**, 141913 (2009).
19 J. He, Surface stress on the effective Young's modulus and Poisson's ratio of isotropic nanowires under tensile load, AIP Adv. **5**, 117206 (2015).
20 P. Chhapadia, P. Mohammadi, and P. Sharma, Curvature-dependent surface energy and implications for nanostructures, J. Mech. Phys. Solids **59**, 2103 (2011).
21 J. Yvonnet, A. Mitrushchenkov, G. Chambaud, and Q. C. He, Finite element model of ionic nanowires with size-dependent mechanical properties determined by ab initio calculations, Comput. Methods Appl. Mech. Eng. **200**, 614 (2011).
22 Y. Liu, X. Ji, D. Wang, and J. He, Modeling thin structures incorporated with surface effects by using layered shell elements, Eur. J. Mech.-A Solids **74**, 139 (2019).
23 Y. Liu, and Y. Wei, Effect of surface energy on the indentation response of hard nanofilm/soft substrate composite structure, Int. J. Mech. Sci. **185**, 105759 (2020).
24 L. Zhang, J. Zhao, G. Nie, and J. Liu, Propagation of Rayleigh-type surface waves in a layered piezoelectric nanostructure with surface effects, Appl. Math. Mech.-Engl. Ed. **43**, 327 (2022).
25 C. Mi, and D. Kouris, Stress concentration around a nanovoid near the surface of an elastic half-space, Int. J. Solids Struct. **50**, 2737 (2013).
26 C. Mi, and D. Kouris, Elastic disturbance due to a nanoparticle near a free surface, Math. Mech. Solids **19**, 868 (2013).
27 C. Mi, Surface mechanics induced stress disturbances in an elastic half-space subjected to tangential surface loads, Eur. J. Mech.-A Solids **65**, 59 (2017).
28 M. Dai, H. B. Yang, and P. Schiavone, Stress concentration around an elliptical hole with surface tension based on the original Gurtin-Murdoch model, Mech. Mater. **135**, 144 (2019).
29 L. H. He, and Z. R. Li, Impact of surface stress on stress concentration, Int. J. Solids Struct. **43**, 6208 (2006).
30 C. Mi, Elastic behavior of a half-space with a Steigmann-Ogden boundary under nanoscale frictionless patch loads, Int. J. Eng. Sci. **129**, 129 (2018).
31 L. Tian, and R. K. N. D. Rajapakse, Analytical solution for size-dependent elastic field of a nanoscale circular inhomogeneity, J. Appl. Mech. **74**, 568 (2007).
32 J. Wang, P. Yan, L. Dong, and S. N. Atluri, Spherical nano-inhomogeneity with the Steigmann-Ogden interface model under general uniform far-field stress loading, Int. J. Solids Struct. **185-186**, 311 (2020).
33 Y. Ban, and C. Mi, Analytical solutions of a spherical nanoinhomogeneity under far-field unidirectional loading based on Steigmann-Ogden surface model, Math. Mech. Solids **25**, 1904 (2020).
34 Z. Y. Ou, and S. D. Pang, Fundamental solutions to Hertzian contact problems at nanoscale, Acta Mech. **224**, 109 (2013).
35 S. Zhou, and X. L. Gao, Solutions of half-space and half-plane contact problems based on surface elasticity, Z. Angew. Math. Phys. **64**, 145 (2013).
36 X. Q. Feng, R. Xia, X. Li, and B. Li, Surface effects on the elastic modulus of nanoporous materials, Appl. Phys. Lett. **94**, 011916 (2009).
37 Z. Lu, F. Xie, Q. Liu, and Z. Yang, Surface effects on mechanical behavior of elastic nanoporous materials under high strain, Appl. Math. Mech.-Engl. Ed. **36**, 927 (2015).
38 R. Xia, X. Q. Feng, and G. F. Wang, Effective elastic properties of

nanoporous materials with hierarchical structure, Acta Mater. **59**, 6801 (2011).
39 L. R. Meza, A. J. Zelhofer, N. Clarke, A. J. Mateos, D. M. Kochochmann, and J. R. Greer, Resilient 3D hierarchical architected metamaterials, Proc. Natl. Acad. Sci. USA **112**, 11502 (2015).
40 V. Tomar, J. Zhai, and M. Zhou, Bounds for element size in a variable stiffness cohesive finite element model, Numer. Meth Eng. **61**, 1894 (2004).
41 Q. Wang, H. Yu, W. L. Xu, C. S. Lyu, J. N. Zhang, M. Micheal, and H. A. Wu, Spatial and temporal constraints of the cohesive modeling: A unified criterion for fluid-driven fracture, Numer. Meth Eng. **124**, 2756 (2023).
42 W. Sun, X. Dong, G. Yu, and L. Shuai, Antibacterial effect of silver nanomaterials on staphylococcal protein a by molecular dynamics simulation, J. Nanosci. Nanotechnol. **20**, 4914 (2020).
43 M. Y. Arsent'ev, Study of the graphitization of the surface of diamond with the orientation of [111] using the method of molecular dynamics, Glass Phys. Chem. **47**, 276 (2021).
44 A. Tsukanov, B. Turk, O. Vasiljeva, and S. Psakhie, Computational indicator approach for assessment of nanotoxicity of two-dimensional nanomaterials, Nanomaterials **12**, 650 (2022).
45 A. R. de Almeida, G. Colherinhas, and D. X. de Andrade, Effects of Coulomb and vdW modifiers on hydrogen-bonds, energy and structural properties of peptide nanomembranes: A study by molecular dynamics simulations, J. Mol. Liquids **382**, 122017 (2023).
46 S. Brach, L. Dormieux, D. Kondo, and G. Vairo, A computational insight into void-size effects on strength properties of nanoporous materials, Mech. Mater. **101**, 102 (2016).
47 Z. Chen, G. Wang, C. Meng, B. Shao, and Y. Shen, Mechanical response of cross-tensioned concrete pavement: Experimental study and finite element, Int. J. Pavement Eng. **24**, 1 (2023).
48 J. Bulling, H. Gravenkamp, and C. Birk, A high-order finite element technique with automatic treatment of stress singularities by semi-analytical enrichment, Comput. Methods Appl. Mech. Eng. **355**, 135 (2019).
49 J. Jung, K. Yoon, and P. S. Lee, Deep learned finite elements, Comput. Methods Appl. Mech. Eng. **372**, 113401 (2020).
50 C. Lee, S. Kim, and P. S. Lee, The strain-smoothed 4-node quadrilateral finite element, Comput. Methods Appl. Mech. Eng. **373**, 113481 (2021).
51 G. Wei, Y. Shouwen, and H. Ganyun, Finite element characterization of the size-dependent mechanical behaviour in nanosystems, Nanotechnology **17**, 1118 (2006).
52 W. F. Wang, X. W. Zeng, and J. P. Ding, Finite element modeling of two-dimensional nanoscale structures with surface effects, Eng. Technol. **4**, 426 (2010).
53 L. Tian, and R. K. N. D. Rajapakse, Finite element modelling of nanoscale inhomogeneities in an elastic matrix, Comput. Mater. Sci. **41**, 44 (2007).
54 D. W. Huang, Size-dependent response of ultra-thin films with surface effects, Int. J. Solids Struct. **45**, 568 (2008).
55 Y. Zhang, C. Mi, and X. Gou, Surface curvature-dependent strength analysis of three-dimensional nanoporous metals, Acta Mech. Sin. **40**, 123314 (2024).
56 A. Y. Zemlyanova, and S. G. Mogilevskaya, Circular inhomogeneity with Steigmann-Ogden interface: Local fields, neutrality, and Maxwell's type approximation formula, Int. J. Solids Struct. **135**, 85 (2018).
57 Y. Zhang, J. Cai, C. Mi, and A. Akbarzadeh, Surface bending resistance in architected nanoporous metallic materials, Advcd Theor. Sims **5**, 2200339 (2022).
58 R. W. Style, R. Boltyanskiy, B. Allen, K. E. Jensen, H. P. Foote, J. S. Wettlaufer, and E. R. Dufresne, Stiffening solids with liquid inclusions, Nat. Phys. **11**, 82 (2015).
59 Y. Wang, and D. L. Henann, Finite-element modeling of soft solids with liquid inclusions, Extreme Mech. Lett. **9**, 147 (2016).
60 J. He, and H. S. Park, A methodology for modeling surface effects on stiff and soft solids, Comput. Mech. **61**, 687 (2017).

考虑表面曲率依赖的纳米材料表面单元设计

张永超, 王连, 王方鑫, 李彬, 苟晓凡

摘要 纳米材料以其显著的表面效应和优异的力学性能而备受关注. 由于理论复杂性, 以往采用有限元方法对纳米材料表面效应研究常简化为较为简单的二维模型, 因此, 不能很好地反映纳米材料的力学性能, 也不能反映表面效应的实质影响, 特别是纳米表面曲率依赖性. 本研究应用最小能量原理, 利用纳米材料Steigmann-Ogden表面理论, 提出了一种综合考虑表面效应的新型有限元表面单, 在此基础上分析了四种典型二维和三维纳米材料模型的应力分布和变形特征. 通过与已有文献的对比, 验证了所提出有限元计算方法的准确性. 所得到的有限元计算方法为精确预测纳米材料力学性能提供了一种可靠和令人信服的科学方法.